Analysis of Slot Coating Flow Under Tilted Die

Semi Lee and Jaewook Nam
Dept. of chemical engineering, Sungkyunkwan University, Suwon, Gyeonggi-do 440-746, Korea

DOI 10.1002/aic.14752
Published online February 25, 2015 in Wiley Online Library (wileyonlinelibrary.com)

Slot coating is a high precision coating method, where the film thickness is controlled by the flow rate fed to the die and the production speed. The range of desirable operating conditions for uniform coating is limited by the shape and locations of upstream and downstream menisci, which are controlled by the pressure gradient within the coating flow. The gradient can be controlled by the shape and orientation of the slot coating die, that is, die configuration. Here, the tilted die, the so-called angle-of-attack configuration is considered. The configuration is similar to underbite and overbite configurations, but it has a sloped die lip due to tilting. Coating flows with such a configuration are examined by computer-aided analysis using the Galerkin/finite element method. Using steady-state analysis, the effect of the angle of attack on the upstream meniscus location is discussed. In transient analysis, the amplitude of the thickness variation is predicted under different types of disturbances, namely flow rate and gap oscillations. The analysis shows that die lip configurations affect the thickness uniformity under periodic disturbances. The effect of die tilting can be similar to or different from the underbite/overbite configurations, depending on the type of oscillation. During the analysis, the flow rate apportioning inside the coating flow and decomposing thickness variations into two separating oscillations are useful in understanding the results is found. © 2015 American Institute of Chemical Engineers *AIChE J*, 61: 1745–1758, 2015

Keywords: slot coating, free surface flow, galerkin/finite element method, periodic disturbance, frequency response analysis, slot-die design

Introduction

The continuous liquid coating process is the method of choice for manufacturing products such as adhesives, magnetic tapes, and optical films. When a highly uniform thin film is produced at a relatively high speed, slot coating is typically preferred. Slot coating is classified as a premetered coating, that is, the final wet film thickness is precisely determined by the flow rate and the production speed and is independent of other process parameters.

A schematic diagram of the slot coating process is shown in Figure 1. Coating liquid is fed into the feed slot and fills the space between the slot die lip and the web. There are two menisci, or gas-liquid interfaces, located upstream and downstream of the coating flow. A liquid bridge bounded by the slot die, web, and menisci is called the coating bead. Typically, vacuum is applied to the upstream coating bead to stabilize it for high-speed production of a thin film.[1]

For a given coating liquid and die design, the shape of the coating bead, that is, the locations and shapes of gas–liquid interfaces, is greatly influenced by operating conditions: web speed, vacuum, and flow rate. In short, these conditions control the balance of forces among viscous, capillary, inertial, and gravity forces. When the balance is maintained, one can achieve desirable flow status, that is, two-dimensional (2-D), steady state, and stable. The map with ranges of desirable operating conditions is called the coating window, and most steady-state coating flow analyses are designed to construct such windows. Starting from pioneering works by Ruschak[2] and Higgins and Scriven,[3] numerous studies for coating windows have been performed. Carvalho and Kheshgi[4] studied low-flow limit. Lee et al.[5] and Chang et al.[6] experimentally determined minimum wet thickness. Lin et al.[7] compared theoretical predictions with experimental observations of coating windows in slot coating system. Recently, the automatic generation method of such windows was proposed by Nam et al.[8] and applied to a variant of slot coating.[9]

However, the coating flow is always surrounded by small-scale disturbances generated by equipment with rotating elements, such as pumps, substrate-driving mechanisms, roll run-outs, and so forth. Because uniformity requirements of films are severe, effects of such small disturbances can be critical. Therefore, the sensitivity analysis of coating flows under such periodic disturbances is important.

Although there have been several previous attempts,[10] experimental research regarding frequency analyses are scarce. Because of natural vibrations, it is extremely difficult to select a target frequency for a specific piece of equipment. Hence, theoretical and computational analyses are preferred. Christodoulou[11] analyzed the frequency response in a slide coating flow. Gates[12] showed various response loops of film thickness and upstream meniscus position against sinusoidal disturbances. Tsuda et al.[13] and Lee et al.[14] used a transient visco-capillary model to predict the effect of periodic

Correspondence concerning this article should be addressed to J. Nam at jaewooknam@skku.edu.

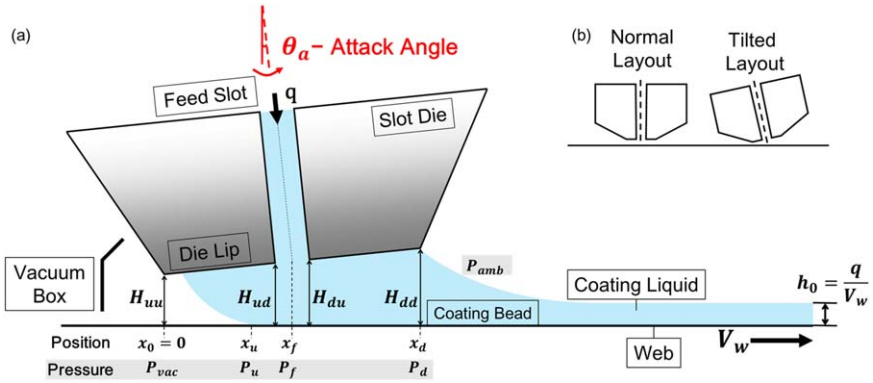

Figure 1. A schematic diagram and parameters for the slot coating flow.

Inset (b) shows a normal layout, where the orientation of the slot die (dashed line) is orthogonal to the web, that is, $\theta_a = 0$, and a tilted layout, where the orientation is nonorthogonal, that is, $\theta_a \neq 0$. Note that basic, underbite, and overbite configurations are classified as the normal layout, and nonzero angle-of-attack configurations are classified as the tilted layout. [Color figure can be viewed in the online issue, which is available at wileyonlinelibrary.com.]

perturbation. Romero and Carvalho[15] solved the transient 2-D Navier–Stokes system to determine the amplitude of thickness variations in slot coating flows. Based on that model, Perez and Carvalho[16] added an optimization algorithm to search for desirable operating conditions.

These analyses have been conducted for numerous die designs, for example, underbite and overbite configurations,[15] but are not sufficiently extensive. For example, several literature[17,18] discussed tilted dies, called an angle-of-attack configuration, but the effect of such a modification has not been examined in detail.

Although such a configuration is easy to achieve in practice,[18] only limited research is available. Sartor[19] performed experimental investigations on such configurations. Gates[12] and Lee et al.[20] analyzed coating defects and response to disturbances of similar configurations using a visco-capillary model, but they did not focus on transient analysis.

Here, we analyze coating flows under the tilted layout, or angle-of-attack configuration, as shown in the inset of Figure 1b. Compared with the normal layout, which has parallel channels between the die lip and moving web, a slight inclined die lip changes the pressure profile due to a lubrication effect. As the upstream and downstream gap heights are different, angle-of-attack configurations are similar to underbite/overbite configurations, which are classified as normal layouts, except sloped die lips. Therefore, it is worthwhile to examine the effect of an angle-of-attack configuration on the coating flows and compare them with those of normal layouts. We first examined the effect of attack angle changes on steady-state coating flows. Then the effects of on-going periodic disturbances on film thickness variations were computationally estimated by analyzing the transient Navier–Stokes system.

Governing Equations and Boundary Conditions

The slot coating flow can be described as a small-scale laminar flow with free surfaces. Therefore, the momentum balance for the flow is governed by an incompressible Navier–Stokes equation

$$\nabla \cdot \mathbf{u} = 0 \tag{1}$$

$$\rho\left(\frac{\partial \mathbf{u}}{\partial t} + \mathbf{u} \cdot \nabla \mathbf{u}\right) - \nabla \cdot \boldsymbol{T} = 0, \tag{2}$$

where $\mathbf{u}$ is the velocity vector, ρ is the liquid density, and $\boldsymbol{T} = -p\boldsymbol{I} + \mu[\nabla \mathbf{u} + (\nabla \mathbf{u})^T]$ is the stress tensor for Newtonian liquid. Here, p is the pressure and μ is the liquid viscosity.

Steady-state formulation

At steady state, Eq. 2 becomes

$$\rho \mathbf{u} \cdot \nabla \mathbf{u} = \nabla \cdot \boldsymbol{T}. \tag{3}$$

Boundary conditions are the same as those in Romero and Carvarho[15] except for the inlet of the feed slot. Details are illustrated on boundary conditions in Figure A1. At the inlet, the flow is assumed to be a parabolic velocity profile

$$u = 0, v = -\frac{6Q}{H_f}\left[\left(\frac{x}{H_f}\right) - \left(\frac{x}{H_f}\right)^2\right], \tag{4}$$

where Q is the flow rate and H_f is the width of the feed slot. For a tilted angle case, the velocity vector $\tilde{\mathbf{u}} = \mathbf{i}\tilde{u} + \mathbf{j}\tilde{v}$ is used instead of $\mathbf{u} = \mathbf{i}u + \mathbf{j}v$, where $\tilde{\mathbf{u}} = \boldsymbol{R} \cdot \mathbf{u}$ with rotation matrix $\boldsymbol{R} = \mathbf{ii}\cos\theta + \mathbf{ij}(-\sin\theta) + \mathbf{ji}\sin\theta + \mathbf{jj}\cos\theta$ and attack angle θ. Here, angle θ increases in the counter-clockwise direction. For our computations, slip coefficient, upstream static contact angle, and dynamic contact angle are $\beta = 0.1\,\mathrm{g^{-1}s^{-1}}$, $\theta_u = 60^\circ$, and $\theta_{dyn} = 120^\circ$, respectively.

Transient formulation—frequency response analysis

The Navier–Stokes Eq. 2 is solved directly for computing a transient response. Following Romero and Carvalho,[15] we considered two types of disturbances: flow rate and gap oscillations

1. Flow rate oscillation. The flow rate per unit width is

$$q(t) = q_0 + q_m \sin(\omega t), \tag{5}$$

where q_0 is a steady-state flow rate, q_m is the amplitude of the sinusoidal disturbance, and ω is the angular frequency represented by $\omega = 2\pi f$ with frequency f. This flow rate is used at the inlet boundary condition.

2. Gap oscillation. At a given base gap height, H_0, and an amplitude, H_m, the imposed periodic oscillation of the gap is

Table 1. Operating Conditions and Parameters Used in this Study

Operating Parameters				
			Base Flow Condition	
Parameter		Range	Steady State	Frequency Response
Density (g/cm^3)	ρ	0.95–1.2	0	1.0
Viscosity (cP)	μ	10–1000	30	30
Surface tension (dyn/cm)	σ	10–60	60	60
Web speed (m/s)	V_w	0.05–5	0.1	0.4
Gap height (μm)	H_0	80–300	100	100
Vacuum pressure (Pa)	P_{vac}	0–5000	500	~8000
Wet thickness (μm)	h_0	10–100	50	20, 50

$$H(t)=H_0-H_m\sin(\omega t). \tag{6}$$

These disturbances lead to a sinusoidal film thickness variation

$$h(t)=h_0+h_m\sin(\omega t+\Phi), \tag{7}$$

where h_0 is the steady-state wet film thickness at the outflow boundary, h_m is the amplitude of the thickness variation, and Φ is the phase lag.

The amplification factors are defined as

$$\alpha_q=\frac{h_m/h_0}{q_m/q_0}\text{ for flow rate oscillation,} \tag{8}$$

$$\alpha_H=\frac{h_m/h_0}{H_m/H_0}\text{for gap oscillation.} \tag{9}$$

The factors represent the ratio of the relative magnitude of film thickness oscillation to the relative magnitude of imposed flow rate and gap height oscillation, respectively.

Operating conditions considered in this study are summarized in Table 1. There are four dimensionless numbers for the coating flows: $N_{Ca}\equiv\mu V_w/\sigma$ (capillary number), $N_{Re}\equiv\rho V_w H_0/\mu$ (Renolds number), $R_{gt}\equiv H_0/h_0$ (gap-to-thickness ratio), and $P^*_{vac}\equiv P_{vac}H_0/\sigma$ (dimensionless vacuum pressure).

Solution Methods

Because the slot coating flow has free boundaries, the flow domain is also unknown *a priori*. Details on the solution method for solving steady-state and transient flows can be found in Romero and Carvalho.[15] Here, we only summarize the important points.

The unknown physical domain, $\mathbf{x}=(x,y)$ is mapped into the reference domain, $\xi=(\xi,\eta)$, which is related by elliptic differential equations

$$\nabla\cdot D_\xi(\xi,\eta)\nabla\xi=0,\nabla\cdot D_\eta(\xi,\eta)\nabla\eta=0, \tag{10}$$

where D_ξ and D_η are mesh diffusivities used to control the node spacing determined by the coordinate potentials ξ and η.

We solved the Navier–Stokes equation using the time derivatives at fixed iso-parametric coordinates

$$\rho[\mathring{\mathbf{v}}+(\mathbf{v}-\mathring{\mathbf{x}})\cdot\nabla\mathbf{v}]-\nabla\cdot\boldsymbol{T}=0, \tag{11}$$

where $\mathring{\mathbf{v}}$ is defined by $\partial\mathbf{v}/\partial t=\mathring{\mathbf{v}}-\mathring{\mathbf{x}}\cdot\nabla\mathbf{v}$, and $\mathring{\mathbf{x}}$ is the mesh velocity, the time derivative of the nodal position.

For predicting several solutions with different angle-of-attack configurations, the arc-length continuation method was used.[21] The method requires the evaluation of the sensitivity of the weighted residual equation, $\mathbf{R}(\mathbf{u},p)=0$, where $\mathbf{u}$ is the solution vector and p is the parameter used in the continuation. For die tilting, the gap height at the upstream or downstream die lip corner is used as the continuation parameter p, instead of the attack angle.

Mesh convergence tests were performed for each flow condition with different angle-of-attack configurations and frequency responses for flow rate and gap oscillation. The final mesh configurations are summarized in Table 2 and mesh configuration details in Figure A2. Note that the optimal mesh configuration of transient flow is different from that of steady-state flow.

Results

Steady-state analysis

Die Geometry and Flow Conditions. Changes in die lip shape can alter flow patterns and menisci shape and location by changing the pressure profile inside the coating bead. The basic die lip configuration for this study has a uniform gap height for both downstream and upstream coating gaps, $H_0=100\,\mu$m. Upstream and downstream die lip lengths are $6H_0$.

The geometries can be categorized into two groups: normal layout, where both die lips are parallel to the web, and tilted layout, where they are not parallel due to tilting, as shown in Figure 1b. Uniform, underbite, and overbite configurations are normal layouts. On the contrary, tilted layouts have diverging or converging channels as shown in positive-angle or negative-angle configurations.

For the computational model, tilted layouts can be achieved by fixing one side of the die lip corner (pivot) and lifting the other outside corner, as shown in Figure 2. The upstream and downstream die lip corners are the pivots for a positive-angle configuration and for a negative-angle configuration, as shown in Figures 2a, b, respectively. The pivots are always located H above the moving web. In this study, the attack angle increases from 0° to 11.09° as the height of the nonpivotal outside die lip corner increases from H to 3.5 H. In reality, the attack angle can be changed by lifting or changing the slot head-to-roll position as discussed in Tracton et al.[18]

Flow conditions for the computational analyses are summarized in Table 1. As the size of the coating bead and the flow rate are small, gravitational and inertial forces are negligible, that is, vanishing density is acceptable.

Effect of Changes in Angle at Steady State. The first solution for the uniform configuration was attained at

Table 2. The Number of Elements and Degrees of Freedom Used in this Study

	Number of Elements	Degrees of Freedom
Geometric continuation	328	6668
Flow rate oscillation	1194	23,586
Gap oscillation	1108	21,936

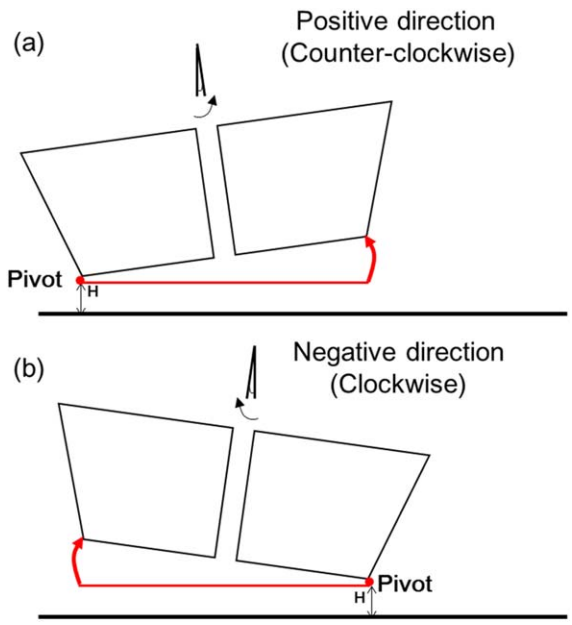

Figure 2. Two possible configurations in a tilted layout: (a) a positive-angle configuration (rotating slot die in the counter-clockwise direction) and (b) a negative-angle configuration (rotating in the clockwise direction).

[Color figure can be viewed in the online issue, which is available at wileyonlinelibrary.com.]

$N_{Ca}=0.05, N_{Re}=0, R_{gt}=2$, and $P^*_{vac}=0.83$. Solutions with different parameter values, such as the gap height at the downstream corner H_{dd} or the upstream corner H_{uu}, are computed using the arc-length continuation discussed in Section Solution Methods.

Figure 3 shows streamlines of the five different angle configurations. In positive angle-of-attack configurations, die tilting affects the upstream meniscus location and the downstream die lip vortex. As the attack angle increases, the upstream meniscus moves toward the feed slot until angle θ_a becomes 1.81° (d) and then moves back toward the upstream outside corner (e). The reason behind this nonlinear meniscus movement will be examined in Section A Simple Model for Upstream Meniscus Location.

When the die tilted more than 1.81°, a vortex is generated under the downstream die lip, as shown in Figure 3e. This strongly suggests that the adverse pressure gradient under the downstream die lip increases as the downstream gap become a diverging channel. At the same time, the size of the upstream bead increases. Details on coating flow changes due to the positive angle of attack are presented in Figure A3.

Unlike positive-angle configurations, the upstream meniscus moves to upstream as the angle decreases, that is, tilts further, in negative-angle configurations. As the angle decreases from b to a, the vortex inside the upstream coating bead appears; and another vortex emerges at the downstream die lip near the feed slot exit. These vortices suggest that there is a strong adverse pressure gradient inside the coating bead, which induces reverse flows due to the converging channel created under the die lips.

There are numerous patents about adjusting die lip shape to prevent coating defects, and some of these patents claims coincide with our results. For example, O'Brien[22] warns that a diverging die configuration may cause dust collection or bubble formations, which implies the formation of a vortex inside the coating bead. Arsten et al.[23] claimed that excessively converging die configurations may lead to coating defects and suggested that the angle needs to be smaller than 30°, but our results indicate that even 10° is excessive. There is a patent that combines die tilting with overbite configuration;[24] it claims that a diverging die with overbite configuration helps to remove bubble formations, but our results strongly suggest that there will be an optimal angle at each given operating condition.

A Simple Model for Upstream Meniscus Location. Well-known defect-causing phenomena such as weeping and bead breakup can be detected based on the location of the upstream meniscus.[9] In other words, predicting the meniscus location can be useful in determining slot coating operating limits. To investigate the nonlinear meniscus movement in positive-angle configurations, we use the one-dimensional (1-D) visco-capillary model proposed by Higgins and Scriven.[3] Variables and parameters for the model are

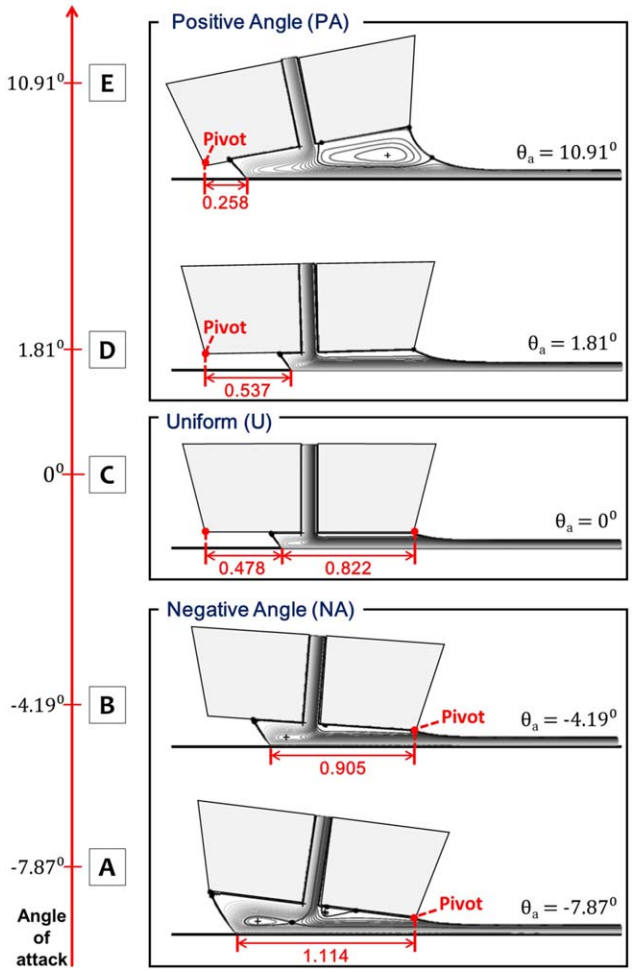

Figure 3. Streamline plots for slot coating flows in different angle-of-attack configurations.

For the pivot point, the outside corner of the upstream die lip and the outside corner of the downstream die lip are chosen for the positive angle case and the negative angle case, respectively. Dimensionless variables for the flows are $N_{Ca}=0.05$, $N_{Re}=0$, and $P^*_{vac}=0.83$. In this steady-state computation, the downstream meniscus, not the upstream meniscus, is pinned. [Color figure can be viewed in the online issue, which is available at wileyonlinelibrary.com.]

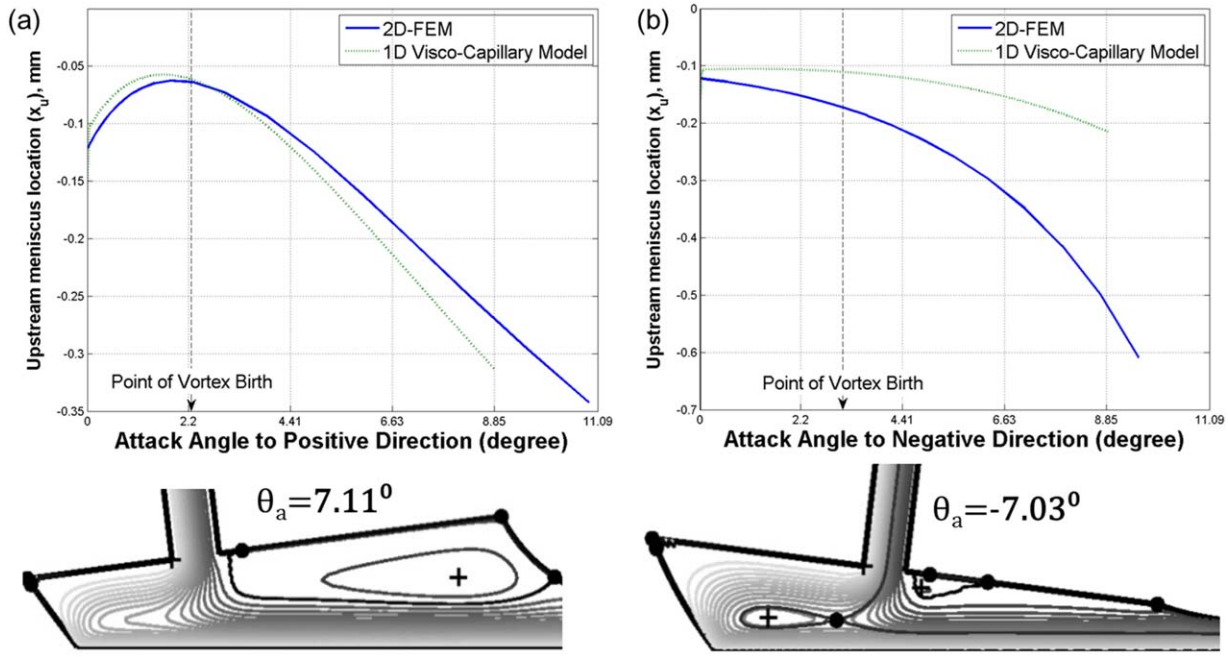

Figure 4. Upstream meniscus location (x_u) with respect to the angle of attack predicted from the visco-capillary model and the finite element computation for (a) positive-angle configuration (PA) and (b) negative-angle configuration (NA).

Note that the DCL location is used as the upstream meniscus location for the finite element computation. Streamline plots below the graphs show vortices inside the coating bead. Dimensionless variables for the flows are $N_{Ca} = 0.05$, $N_{Re} = 0$, $R_{gt} = 2$, and $P^*_{vac} = 0.83$. [Color figure can be viewed in the online issue, which is available at wileyonlinelibrary.com.]

shown in Figure 1. At a given geometry, the gap height profile can be expressed as $h(x)=H_{uu}+(H_{dd}-H_{uu})x/L(x_u)$, where $L(x_u)=x_d-x_u$ is the upstream coating bead length that varies with die tilting. From the model, the upstream meniscus location x_u can be derived as

$$x_u=\frac{L(x_u)}{H_{dd}-H_{uu}}\left[\frac{6\mu V_w L(x_u)h(x_f)}{(P_f-P_u)(H_{dd}-H_{uu})h(x_f)+6\mu V_w L(x_u)}-H_{uu}\right]. \quad (12)$$

One can derive the above equation from the model described in Chapter 5 of Gates.[12] This nonlinear equation is solved iteratively by Newton's method.

Figure 4 shows the effect of angle of attack on the upstream meniscus location predicted from 2-D finite element computation and 1-D visco-capillary model. In the small angle regime, that is, $\theta_a < 2.2^\circ$, the meniscus advances toward the feed slot (or an increasing y axis direction) as the angle increases slightly, as shown in Figure 4a. However, the trend reverses, that is, the meniscus retreats, as the die rotates further in the counter-clockwise direction.

This nonlinear meniscus movement is closely related to changes in the upstream coating bead pressure profile due to the upstream meniscus shape change. In the model, the upstream meniscus curvature R_c is derived as

$$R_c=-\frac{\sigma}{h(x_u)}\left[\cos\theta_{dyn}+\cos(\theta_u-\theta_a)\right]$$

where σ, θ_{dyn}, θ_u, and θ_a are surface tension, dynamic contact angle, static contact angle, and angle of attack, respectively. Here, $\theta_{dyn}=120^\circ$ and $\theta_u=60^\circ$. Therefore, the curvature is a function of θ_a and $h(x_u)$ only. Note that the sign of the curvature only depends on θ_a because $h(x_u)$ is always positive. Consequently, the shape of the meniscus changes with θ_a

$$\begin{cases} \theta_a > 0 & \Rightarrow & R_c < 0 & \text{(convex)} \\ \theta_a = 0 & \Rightarrow & R_c = 0 & \text{(flat)} \\ \theta_a < 0 & \Rightarrow & R_c > 0 & \text{(concave)} \end{cases}$$

Therefore, the pressure at the upstream meniscus P_u in the positive-angle configuration is always less than the vacuum pressure due to the shape of the meniscus. Furthermore, P_u decreases as angle θ_a increases, as shown in Figure 5.

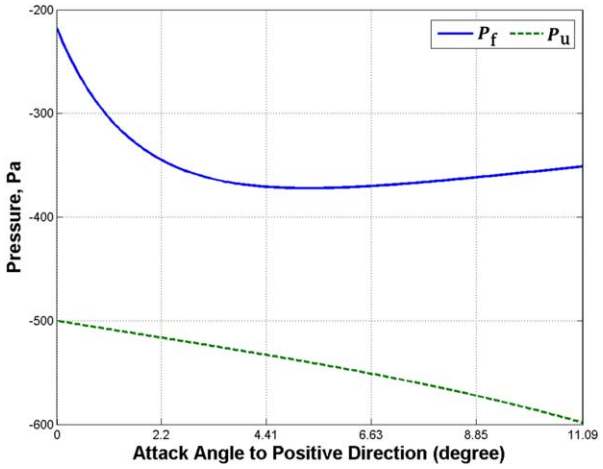

Figure 5. Pressure changes at the feed slot exit P_f and the upstream meniscus P_u with respect to the positive angle of attack.

The results are predicted from the visco-capillary model. $N_{Ca} = 0.05$, $N_{Re} = 0$, $R_{gt} = 2$, and $P^*_{vac} = 0.83$ [Color figure can be viewed in the online issue, which is available at wileyonlinelibrary.com.]

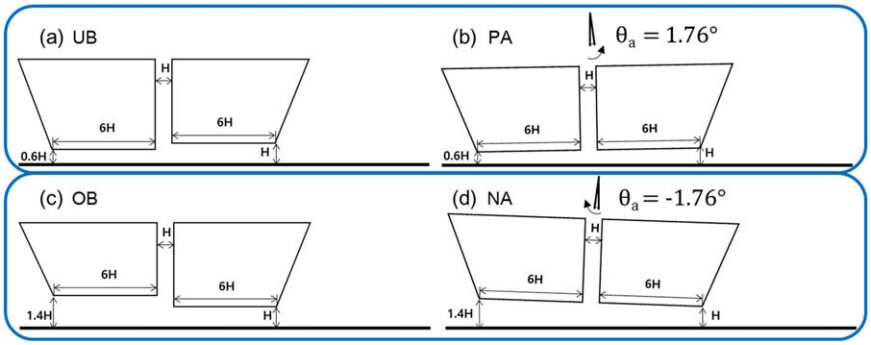

Figure 6. Two pairs of comparable geometries.

The first pair has a small upstream coating gap: (a) underbite (UB) and (b) positive-angle (PA) configurations. The second pair has a large upstream coating gap: (c) overbite (OB) and (d) negative-angle (NA) configurations. [Color figure can be viewed in the online issue, which is available at wileyonlinelibrary.com.]

Meanwhile, the feed slot exit pressure P_f decreases rapidly as θ_a increases but then approaches a plateau with gradually increasing pressure value. Note that the distance between the feed slot exit and the moving web increases as θ_a increases; this increasing channel size is responsible for rapid decreases of pressure at a small θ_a value. However, when θ_a is large enough, the adverse pressure gradient caused by the diverging channel due to tilting controls the pressure profile near the feed slot exit and is responsible for the gradual increases in P_f. Consequently, the pressure difference (P_f–$P_{u)}$ should pass through the minimum around $\theta_a \sim 2.2°$. Therefore, the dominant factors for the nonlinear response are the two competing pressures, P_f and P_u.

For the negative-angle configuration, the upstream meniscus location decreases monotonously as θ_a decreases or H_{uu} increases. However, there is a significant deviation in the meniscus location predicted from the visco-capillary model and the finite element computation, as shown in Figure 4b. Because of a large 2-D flow vortex inside the upstream coating bead, the pressure field under the upstream die lip cannot be precisely predicted by the visco-capillary model. As the meniscus location is sensitive to the pressure field, deviation is inevitable. Therefore, care is needed when predicting operating limits, such as bead breakup and weeping, using the visco-capillary model for the negative-angle configuration.

Frequency response (transient analysis)

Comparable Geometries. The effect of die lip configuration on film thickness variation under on-going periodic disturbances are examined using the transient finite element computation. We are particularly interested in the comparisons between normal and tilted layouts: underbite vs. positive-angle configurations and overbite vs. negative-angle configurations. For fair comparison, the gap heights at upstream and downstream die lip corners are the same for each pair of comparable configurations, as shown in Figure 6. From now on, uniform, underbite, overbite, positive-angle, and negative-angle configurations are abbreviated as U, UB, OB, PA, and NA, respectively.

Operating conditions for the transient analysis are summarized in Table 1. Here, the dimensionless vacuum pressure P^*_{vac} for each configuration is adjusted to maintain the same steady-state upstream meniscus location close to the upstream die lip corner.

To estimate the effect of on-going disturbances on film uniformity, we impose flow rate and gap periodic oscillations to initially steady-state flow states and measure temporal film thickness changes at the outflow boundary.

Flow Rate Oscillation. As discussed in Romero and Carvalho,[15] both upstream and downstream menisci fluctuate to accommodate the surplus and deficit of liquid caused by the flow rate oscillations. They showed that the amplitudes of upstream meniscus are strongly affected by the flow resistance under the upstream coating bead, which can be controlled by the die configuration. In this study, frequency response analysis for the flow rate oscillation is performed at $N_{Ca} = 0.2$, $N_{Re} = 1.33$, $R_{gt} = 5$, and $q_m = 0.05\ q_0$. To maintain the same upstream bead size, P^*_{vac} is selected to 13.33, 26.33, 21.87, 9.93, and 10.05 for U, UB, PA, OB, and NA, respectively.

The amplification factors, α_q, for all configurations with respect to disturbance frequency are presented in Figure 7. Compared with UB, PA shows a slightly smaller amplification factor in the range of 10–800 Hz. On the contrary, NA shows a slightly larger amplification factor than OB, as shown in Figure 7. Note that, when the disturbance frequency is too high (over 1000 Hz), the flow oscillations are quickly damped by viscous dissipation, and the amplification factors vanish

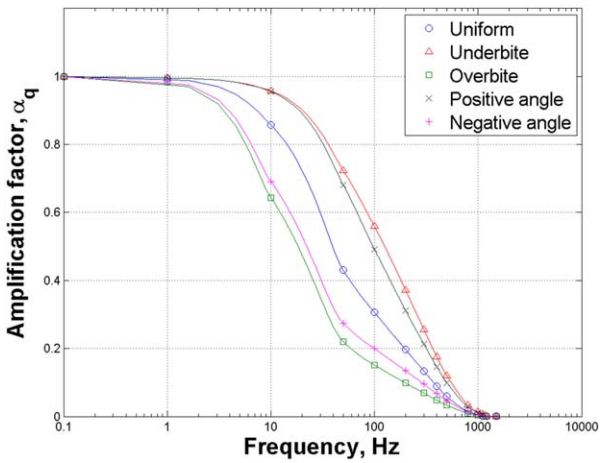

Figure 7. Amplification factor α_q as a function of the frequency of the flow rate oscillation.

The computations were performed at $N_{Ca} = 0.2$, $N_{Re} = 1.33$, $R_{gt} = 5$, and $q_m = 0.05\ q_0$. P^*_{vac} =13.33 (U), 26.33 (UB), 21.87(PA), 9.93 (OB), and 10.05 (NA). [Color figure can be viewed in the online issue, which is available at wileyonlinelibrary.com.]

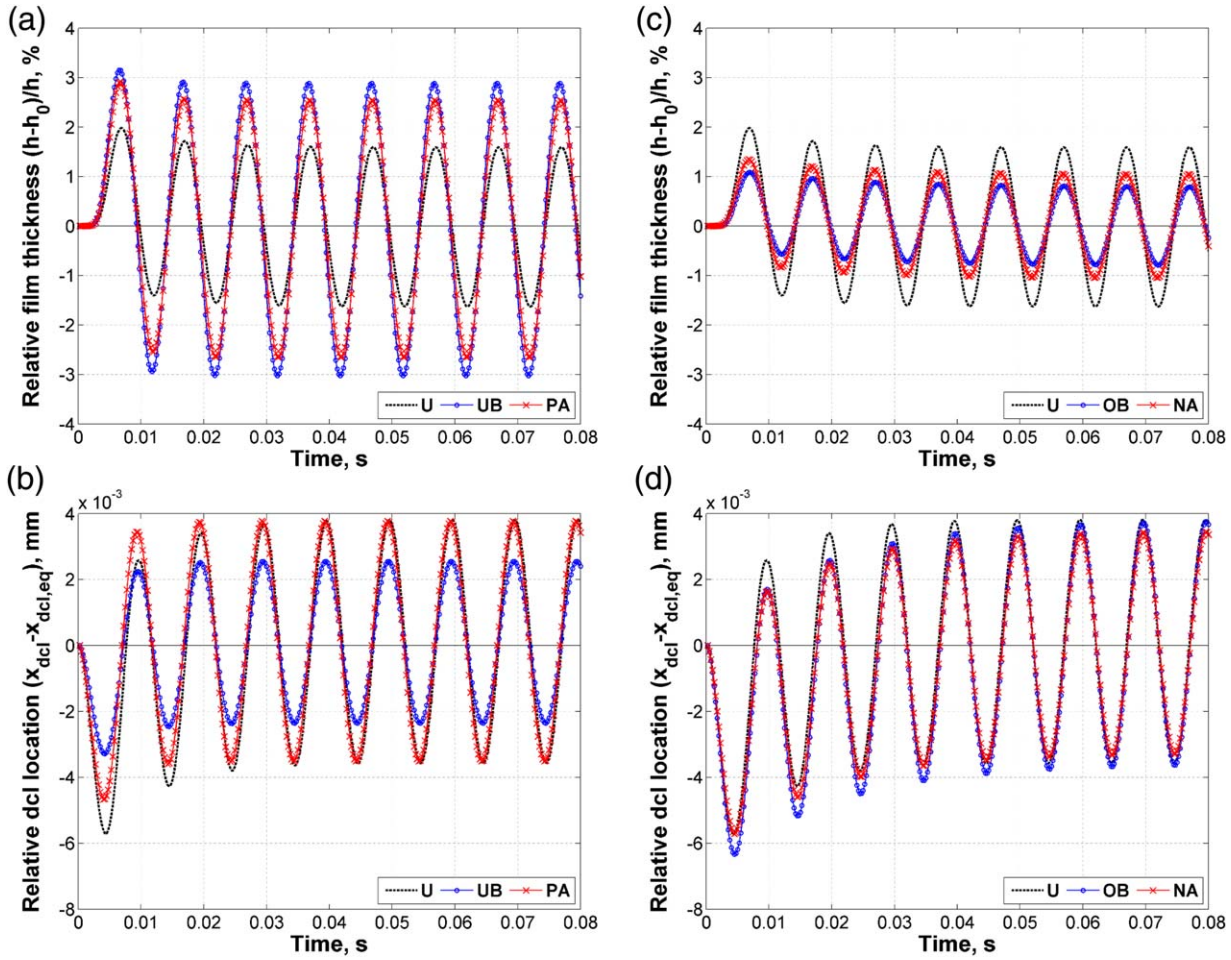

Figure 8. The relative film thickness variation with respect to the steady-state thickness h_m (upper two plots) and the movement of the DCL with respect to the steady-state location (lower two plots) under a given flow rate oscillation ($f = 100$ Hz).

Plots (a) and (b) show the comparison between underbite and positive-angle configurations; and plots (c) and (d) show the comparison between overbite and negative-angle configurations. $N_{Ca} = 0.2$, $N_{Re} = 1.33$, $R_{gt} = 5$, and $q_m = 0.05$ q_0; $P^*_{vac} = 13.33$ (U), 26.33 (UB), 21.87(PA), 9.93 (OB), and 10.05 (NA). [Color figure can be viewed in the online issue, which is available at wileyonlinelibrary.com.]

regardless of die configuration. Consequently, higher frequency flow rate disturbances, that is, using a smaller gear size, is favorable for maintaining higher film uniformity.

Figure 8 represents film thickness variations related to downstream free surface movements, and dynamic contact line (DCL) motions related to upstream meniscus movements, at the flow rate oscillation 100 Hz. UB has the smaller upstream coating gap profile, and consequently causes smaller upstream bead volume per unit width; and this is accompanied by a higher flow resistance than that of PA. This higher flow resistance leads to the smaller upstream meniscus movement, as shown in Figure 8b. At the same time, the flow rate disturbance is not substantially absorbed due to the smaller upstream coating bead volume. Therefore, the more portion of the disturbance propagates to the downstream direction and leads to larger thickness variations, as shown in Figure 8a. However, the difference in the amplitudes of the thickness variation between UA and PA is not as substantial as that of upstream meniscus movement.

When OB and NA are compared as shown in Figures 8c, d, NA has smaller upstream bead volume, smaller upstream meniscus movement, and larger thickness variations than OB. The difference in the upstream meniscus movement between OB and NA is not significant, because the upstream bead volumes in both configurations are already large enough, as shown in Figures 6c, d. Therefore, the channel shape cause by the tilted die lip slope does not significantly contribute to a pressure gradient, and it takes a long time to reach steady oscillations of upstream meniscus movement. Compare Figures 8b–d.

Table 3 exhibits the flow rate apportioning from the feed slot for different configurations, where $\bar{q}_u$ and $\bar{q}_d$ are the

Table 3. Effect of Configuration on Flow Rates Toward Upstream ($\bar{q}_u$) and Downstream ($\bar{q}_d$) Directions for Different Configurations

Configuration	$\bar{q}_u/q_0$	$\bar{q}_d/q_0$
UB	0.4462	0.5539
PA	0.4715	0.5285
U	0.7426	0.2574
NA	0.9102	0.0898
OB	1.0000	0.0000

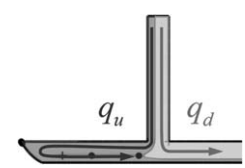

Note that the flow rates are averaged over one cycle of oscillation.

Table 4. Changes in Both Upstream ($\bar{q}_u/q_0$) and Downstream ($\bar{q}_d/q_0$) Flow Rate Ratios and Upstream ($\tilde{G}_{u,m}$) and Downstream ($\tilde{G}_{u,m}$) Pressure Gradient Fluctuation Amplitudes According to Dimensionless Film Thickness (h_w^*)

h_w^*	$\bar{q}_u/q_0$	$\tilde{G}_{u,m}$	$\bar{q}_d/q_0$	$\tilde{G}_{d,m}$
0.20	0.67	0.1780	0.33	0.1283
0.25	0.56	0.1701	0.44	0.1375
0.30	0.49	0.1644	0.51	0.1440
0.35	0.45	0.1604	0.55	0.1484
0.40	0.41	0.1576	0.59	0.1515
0.45	0.38	0.1556	0.62	0.1536
0.50	0.36	0.1543	0.64	0.1551

average flow rate toward upstream and downstream coating beads, respectively. For computing $\bar{q}_u$ and $\bar{q}_d$, we first find the separating streamlines that pass through the cusp point of the streamline under the upstream die lip and reach the inlet boundary.[8] Then, the flow rate at the inlet boundary can be divided into left and right sides of the separating streamline, and their average values over a single cycle, when they reach steady oscillations, are referred to as $\bar{q}_u$ and $\bar{q}_d$, respectively. In general, a smaller upstream channel will provide more flow resistance that results in smaller $\bar{q}_u$ and larger $\bar{q}_d$. Note that OB has vanishing $\bar{q}_d$ and produces films with the highest degree of uniformity.

From the above results, the smaller downstream free surface movement, which is directly related to the film thickness variation, and the larger upstream meniscus movement; both coincide with smaller $\bar{q}_d$ and larger $\bar{q}_u$ caused by the larger upstream coating bead volume per unit width due to the die lip configurations. However, the flow rate apportioning is not only controlled by the die lip configurations but also the operating conditions, such as the average overall flow rate q_0. Table 4 showed that $\bar{q}_d$ and $\bar{q}_u$ can be controlled via q_0 even in U (uniform) configuration, when the web speed is fixed. $\bar{q}_d$ and $\bar{q}_u$ are proportional and inversely proportional to the flow rate, respectively. Note that $\bar{q}_0=\bar{q}_u+\bar{q}_d$.

For thinner film production, q_0 is smaller and a higher vacuum is required to maintain the upstream bead. This strong vacuum pressure not only pulls the upstream meniscus, but also strengthens the pressure gradient to increase q_u and consequently decrease q_d, because q_0 is fixed in slot coating flows. In this study, $f=100\,\text{Hz}, N_{Ca}=0.2$, $N_{Re}=1.33$, and $q_m=0.05\ q_0$, that is, 5% flow rate disturbance. In U configuration, the gap-to-film thickness R_{gt} is decreased from 5 to 2, that is, the dimensionless thickness $h_w^*=h_w/H_0$ is increased from 0.2 to 0.5. Vacuum is adjusted with respect to a given q_0 such that the steady-state upstream bead size is the same for different film thickness.

To make fair comparisons, we normalize amplitudes

$$\tilde{h}=\frac{h_m}{h_0}\ \text{normalized film thickness oscillation amplitude}$$

$$\tilde{G}_{u,m}=\frac{G_{u,m}}{G_{f,m}}\ \text{normalized upstream pressure gradient amplitude}$$

$$\tilde{G}_{d,m}=\frac{G_{d,m}}{G_{f,m}}\ \text{normalized downstream pressure gradient amplitude,} \tag{13}$$

where $G_{u,m}$ is the pressure gradient oscillation amplitude measured at the fully developed flow section of the upstream coating bead, $G_{d,m}$ is the pressure gradient oscillation amplitude measured at the fully developed flow section of the downstream coating bead, and $G_{f,m}$ is the pressure gradient oscillation amplitude due to the flow rate oscillation at the inlet boundary. Note that all oscillatory behaviors are fitted to sine functions to extract the corresponding amplitudes. As responses to the flow rate oscillation are linear at low capillary and Reynolds numbers,[15] these normalized amplitudes represent the relative strengths of disturbances under given flow rate oscillations: larger values represent relatively stronger oscillation effects.

Figure 9 correlates the normalized thickness variations with respect to normalized amplitudes. The results show that the amplitude of the relative thickness oscillation $\tilde{h}$ is inversely proportional and directly proportional to the upstream and the downstream pressure gradient oscillations, respectively. Clearly, the upstream pressure gradient oscillation causes the upstream meniscus motion, and the upstream coating bead acts as a damper: the larger upstream meniscus

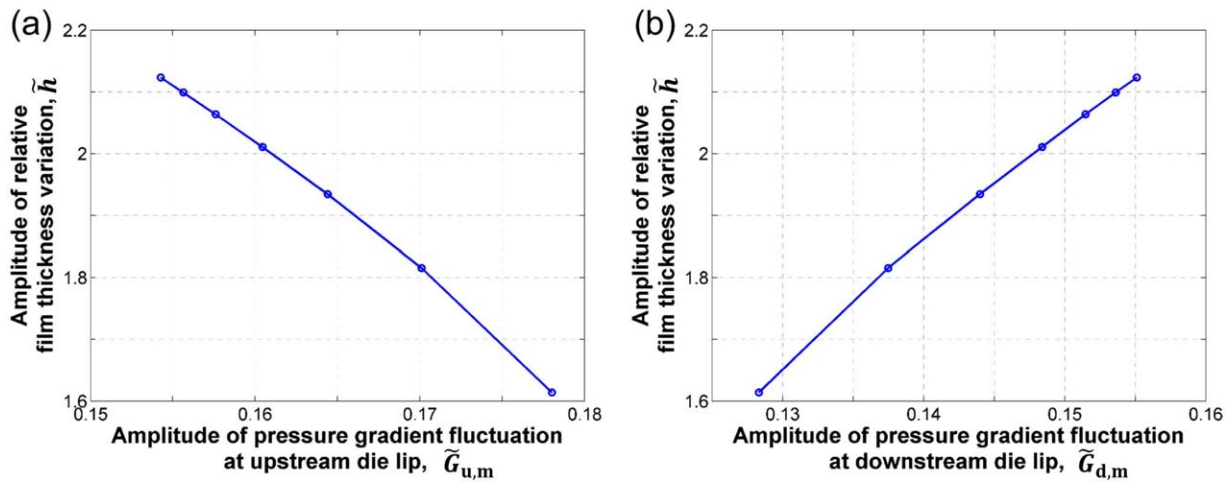

Figure 9. The relationship between film thickness variation $\tilde{h}$ and pressure gradient fluctuation at upstream $\tilde{G}_{u,m}$, and downstream $\tilde{G}_{d,m}$, described in Eq. 13.

The computations were done at $N_{Ca}=0.2$, $N_{Re}=1.33$, and $q_m=0.05\ q_0$. The vacuum was adjusted to match the same upstream bead size: P_{vac}^* =13.33 ($h_w^*=20$), 12.23 ($h_w^*=25$), 11.15 ($h_w^*=30$), 10.15 ($h_w^*=35$), 9.21 ($h_w^*=40$), 8.29 ($h_w^*=45$), and 7.39 ($h_w^*=50$). [Color figure can be viewed in the online issue, which is available at wileyonlinelibrary.com.]

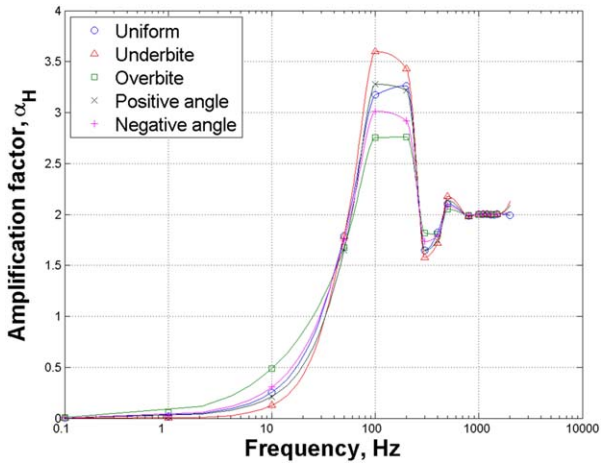

Figure 10. The amplification factor α_H as a function of the frequency of the gap oscillation.

The computations were performed at $N_{Ca} = 0.2$, $N_{Re} = 1.33$, $R_{gt} = 2$, $H_m = 0.05\ H_0$, and P^*_{vac} =7.42 (U), 20.33 (UB), 14 (PA), 3.83 (OB), and 5.08 (NA). [Color figure can be viewed in the online issue, which is available at wileyonlinelibrary.com.]

oscillation leads to the smaller thickness variation. The downstream pressure gradient directly influences the thickness variation directly by perturbing the downstream meniscus attached to the downstream die lip.

By comparing Table 4 with Figure 9, one can conclude that the flow rate apportioning is strongly related to these pressure gradients under die lips. The pressure gradients can be controlled not only by operating conditions, such as overall flow rate or vacuum pressure, but also die lip configurations. Therefore, the smaller amplification factors for OB and NA can be explained by the smaller pressure gradient oscillations under the downstream die lips. Due to the flow rate apportioning, the pressure gradient under the upstream die lip oscillates more, which in turn larger upstream meniscus movement, than other configurations.

Furthermore, Table 4 and Figure 9 lead to another interesting conclusion: for the flow rate oscillation, operating conditions of a thin film more efficiently suppress thickness disturbance than those of a thick film. However, increasing vacuum pressure can increase the magnitude of the vacuum disturbance, which may threaten film uniformity.

Gap Oscillation. Frequency response analysis of the gap oscillation is performed at $N_{Ca} = 0.2$, $N_{Re} = 1.33$, $R_{gt} = 2$, and $H_m = 0.05H_0$, that is, 5% gap disturbance. To maintain the same upstream coating bead size at the initial condition, the vacuum pressure P^*_{vac} is adjusted to 7.42, 20.33, 14, 3.83, 5.08 for U, UB, PA, OB, and NA, respectively.

The amplification factor α_H with respect to disturbance frequency are presented in Figure 10. In all configurations, α_H increases as f increases, reaches the maximum value near $f \approx 100$ Hz, and asymptotically approaches 2. Unlike those of flow rate oscillation, the amplification factors of gap oscillation exceed 1 over 50 Hz. Furthermore, there is no optimal configuration, that is, showing the smallest α_H, over all frequency ranges: UB is the best near $f \approx 10$ Hz, but OB become the winner near $f \approx 100$ Hz. In sum, there are two noticeable differences from α_q:

1. the effects of configuration are different near $f \approx 10$ Hz and $f \approx 100$ Hz,
2. there is a secondary peak near $f \approx 500$ Hz.

These observations cannot be easily understood by considering the thickness variations alone.

Unlike the flow rate oscillation, the film thickness is not only determined by the downstream free surface shape, but also the vertical location of the web. Figure 11 shows the film thickness variation at $f = 200$ Hz. Note that the free surface does not oscillate in phase with the web. In this particular case, the motions completely out of phase lead to larger

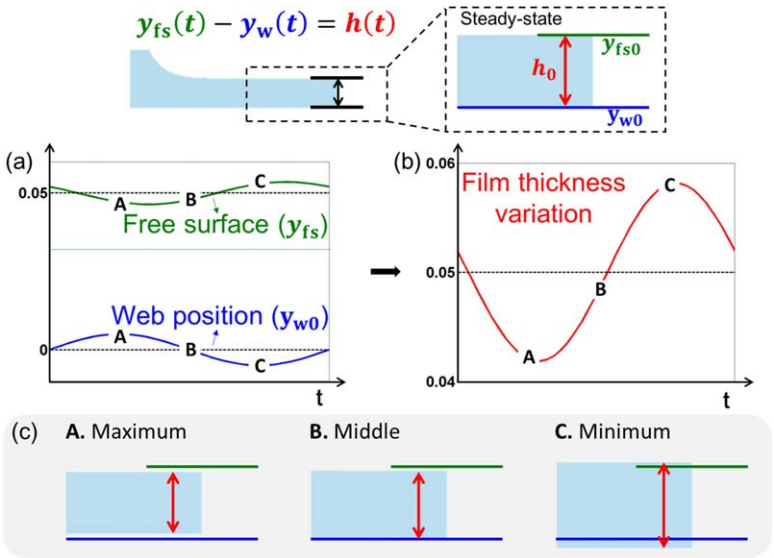

Figure 11. The graphs of (a) input web oscillation and response of free surface, and (b) the result of film thickness variation in one cycle ($f = 200$ Hz).

The final film thickness is determined by the distance between the free surface and web. Note that the free surface does not always move in conjunction with the web. Inset (c) shows snapshots of the film at the outflow boundary obtained at maximum, middle, and minimum points of the web oscillation, that is, A, B, and C points in inset (a). $N_{Ca} = 0.2$, $N_{Re} = 1.33$, $R_{gt} = 2$, and $H_m = 0.05\ H_0$; P^*_{vac} =7.42 (U), 20.33 (UB), 14 (PA), 3.83 (OB), and 5.08 (NA). [Color figure can be viewed in the online issue, which is available at wileyonlinelibrary.com.]

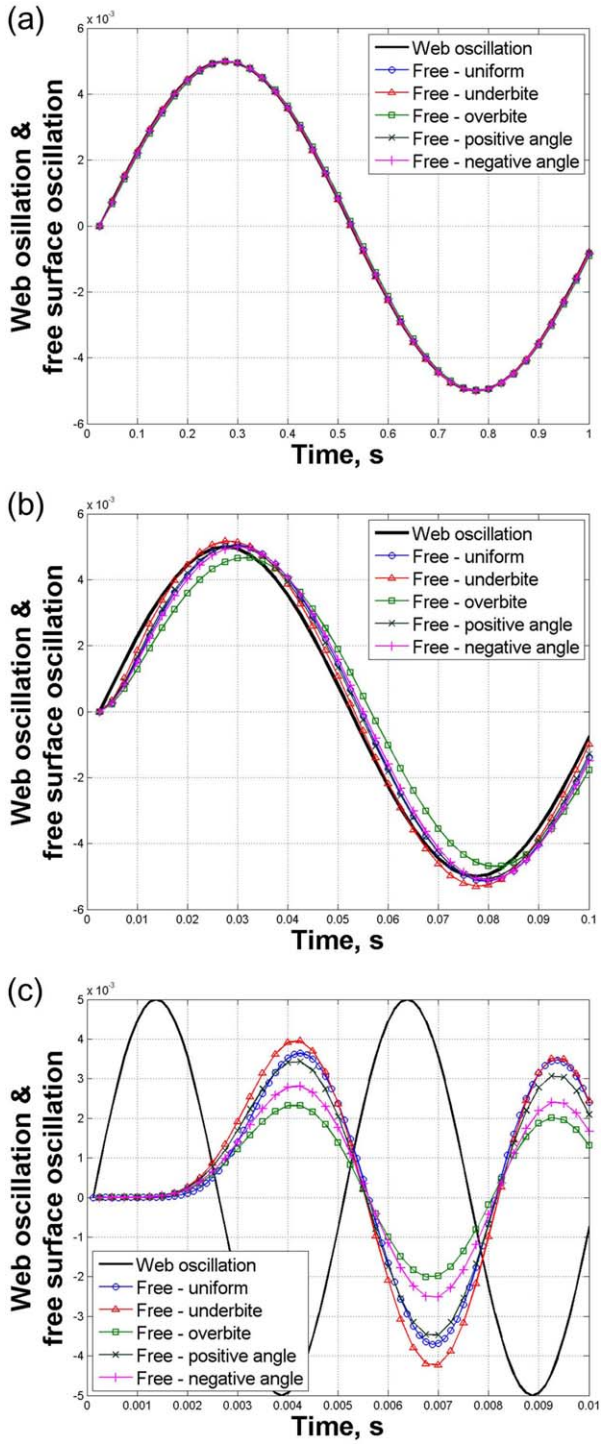

Figure 12. The outflow free surface oscillation relative to its steady location, and the location of web oscillating with (a) 1 Hz, (b) 10 Hz, and (c) 200 Hz.

$N_{Ca} = 0.2$, $N_{Re} = 1.33$, $R_{gt} = 2$, $H_m = 0.05$ H_0; and P^*_{vac} =7.42 (U), 20.33 (UB), 14 (PA), 3.83 (OB), and 5.08 (NA). [Color figure can be viewed in the online issue, which is available at wileyonlinelibrary.com.]

film thickness oscillation than free surface oscillation, as shown in Figure 11b.

Figure 12 shows the outflow free surface location relative to its steady value and the location of the web over time with respect to $f = 1$, 10, and 200 Hz. For $f = 1$ Hz (Figure 12a), there is virtually no phase lag between the free surface and the web, and the magnitudes are the same, that is, the flow reaches a quasi-steady state. A visible phase lag appears at $f = 10$ Hz (Figure 12b), and OB has the most significant phase lag and a noticeable yet small decrease in the amplitude. The phase lag reaches π at $f\ \pi$ 200 Hz (Figure 12c): the crest of the free surface oscillation occurs at the trough of the web oscillation.

These two oscillations, the free surface location y_{fs} and web location $y_{w,}$ can be expressed as

$$y_w(t) = y_{w0} + y_{wm}\sin(\omega_w t), \tag{14}$$

$$y_{fs}(t) = y_{fs0} + y_{fsm}\sin(\omega_{fs} t + \Phi_{fsw}), \tag{15}$$

where y_{w0}, y_{wm}, y_{fs0}, y_{fsm}, ω_w, ω_{fs}, and Φ_{fsw} are the steady web location, the web oscillation amplitude, the steady free surface location, the free surface oscillation amplitude, the angular frequency of web, the angular frequency of free surface, and the phase lag between the web and the free surface oscillations, respectively. Note that Φ_{fsw} is different from the phase lag for the film thickness Φ in Eq. 7. Then, we introduce the amplification factor for the free surface amplitude as

$$\alpha_{fs} = \frac{y_{fsm}/H_0}{y_{wm}/H_0}. \tag{16}$$

The amplification factor α_{fs} as a function of the frequency for all configurations is presented in Figure. 13. The figure shows that the amplitude of free surface oscillation increases in the order of OB, NA, U, PA, and UB. Like the flow rate oscillation, there are two limits: quasi-steady regime at low frequency ($f \lesssim 3$ Hz) and highly damped regime at high frequency ($f \gtrsim 700$ Hz). In between, at 3 Hz $\lesssim f \lesssim$ 700 Hz, the effect of die lip configurations become prominent. OB and NA always damp the free surface oscillation, whereas U, PA, and UB can amplify the oscillation in a certain range. As pointed out by Romero and Carvalho,[15] the smaller upstream channel, for example, UB, has a stronger pressure gradient that leads to larger free surface oscillation.

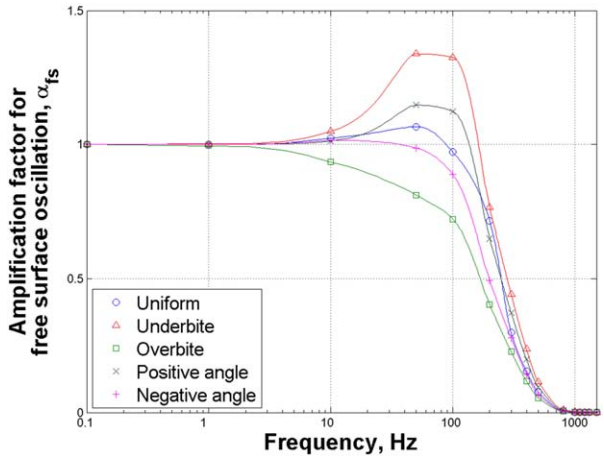

Figure 13. The amplification factor for free surface oscillation α_{fs} as a function of the frequency of the gap oscillation.

Note that this factor only reflects the free surface movement, not the film thickness variation. $N_{Ca} = 0.2$, $N_{Re} = 1.33$, $R_{gt} = 2$, and $H_m = 0.05$ H_0; P^*_{vac} =7.42 (U), 20.33 (UB), 14 (PA), 3.83 (OB), and 5.08 (NA). [Color figure can be viewed in the online issue, which is available at wileyonlinelibrary.com.]

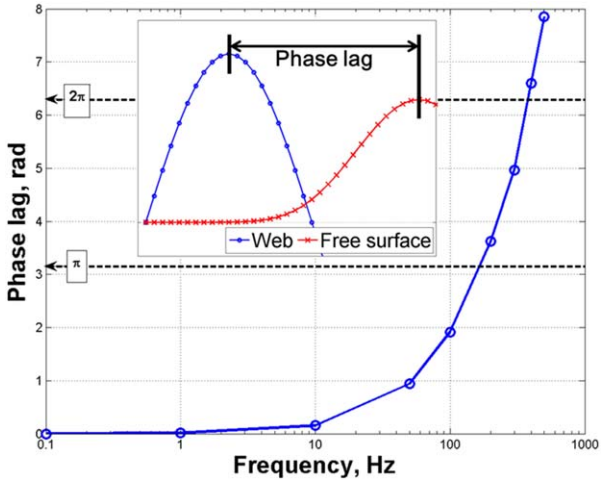

Figure 14. The phase lag of the free surface with respect to the oscillating web Φ_{fsw} as a function of the frequency of the gap oscillation in the uniform configuration.

Other configurations also show similar trend. $N_{Ca} = 0.2$, $N_{Re} = 1.33$, $R_{gt} = 2$, and $H_m = 0.05\ H_0$; P^*_{vac} =7.42 (U), 20.33 (UB), 14 (PA), 3.83 (OB), and 5.08 (NA). [Color figure can be viewed in the online issue, which is available at wileyonlinelibrary.com.]

Comparing PA and UB, the additional pressure gradient due to diverging channels created by tilting damps the free surface oscillation. Note that, near $f = 200$ Hz, the amplification factor for PA is even below that for U. However, the converging channel amplifies the free surface oscillation, when NA and OB are compared. Unlike the flow rate oscillation, the gap oscillation has a significant effect on the free surface oscillation, as shown comparing Figures 7 and 13.

The phase lag between the free surface and the web oscillations also changes, as shown in Figure 14. The phase lag becomes visible around $f \approx 10$ Hz, increases as the frequency increases, and eventually passes though 2π (one complete cycle) around $f \approx 400$ Hz. As pointed out in Figure 12, the phase lag becomes π (half of a cycle) around $f \approx 200$ Hz.

Because $h(t) = y_{fs}(t) - y_w(t)$, the film thickness depends not only on the magnitude of the free surface oscillation but also on the phase lag of the free surface. Considering Figures 13 and 14, the largest thickness variation appears around $f = 100 \sim 200$ Hz for all configurations.

The two distinct features of α_H in Figure 10 in comparison with α_q can be explained by the free surface amplitude (Figure 13) and the phase lag (Figure 14). Near $f \approx 10$ Hz, α_H is relatively small, and only OB shows a large amplification factor. In this low frequency, α_{fs} and Φ_{fsw} of each configuration do not vary much, except in OB. It has not only small α_{fs} but also large Φ_{fsw} as shown in Figure 12b. Note that the configurations with tilted configurations (PA and NA) oscillate almost in phase and with a similar magnitude to U. Therefore, free surface oscillation in the OB configuration deviates significantly from the web. Although the effect of a larger upstream channel can damp the free surface oscillation as shown in Figure 13, the phase lag can increase the film thickness variation.

Near $f \approx 100$ Hz, free surface oscillation amplitude is significantly affected by the die lip configuration as shown in Figure 13. However, the differences between the phase lags from each configuration become hardly noticeable and the lags are close to π (Figure 12c). In this frequency range, the configurations with a larger upstream bead volume, for example, OB and NA, suppress the thickness variation better than other configurations. Although channel shapes are different, α_H for PA is virtually the same as that for U. Apparently, the additional pressure gradient caused by diverging channel shape of PA shifts Φ_{fsw} to counteract the free surface amplitude increase.

The relationship between the free surface and web oscillations also reveals the secondary peak near $f \sim 500$ Hz, as shown in Figure 10. In this regime, the phase lag passes beyond 2π (one cycle) such that the alignment between the free surface and web oscillations reappears. However, the free surface oscillation is dampened significantly, as shown in Figure 13. Therefore, the peak is smaller than the primary peak. Note that this secondary peak is not reported in Romero and Carvalho.[15] Tsuda et al.[13] reported it (and even a third peak), although they explained it using the resonance phenomena of capillary waves using their modal analysis. We did not attempt to produce the third peak, mainly due to the very small time step needed for the time integration. However, we expect that the third peak is obtainable and is also caused by the phase lag.

Another important oscillation occurs at the upstream meniscus. The amplitude of the upstream meniscus oscillation with respect to its steady location is depicted in Figure 15. Unlike the flow rate oscillation, the upstream coating bead cannot act as a damper because the oscillation is produced by the entire web surface. When the upstream meniscus oscillates significantly, it may be difficult to maintain uniform meniscus shape in the cross-flow direction. Under such circumstances, the upstream meniscus may become nodular (inset of Figure 15), which can redistribute flows inside the coating bead and can disrupt the cross-web film uniformity.

Final Remarks

In this study, we present a computational analysis of the effect of angle of attack in the slot coating flow. According to the steady-state analysis, changes in die configurations at

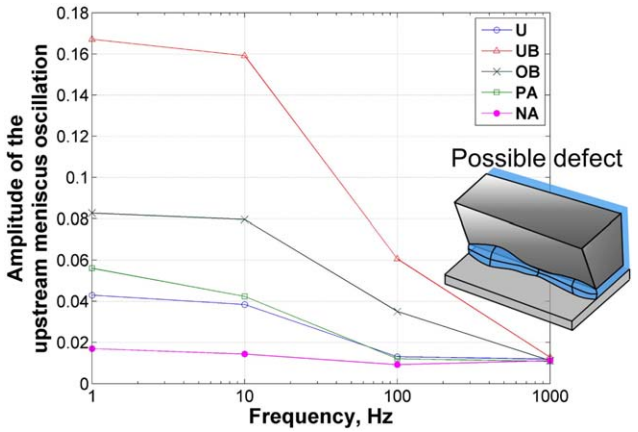

Figure 15. The amplitude of the upstream meniscus oscillation as a function of the frequency of the gap oscillation.

$N_{Ca} = 0.2$, $N_{Re} = 1.33$, $R_{gt} = 2$, $H_m = 0.05\ H_0$, and P^*_{vac} =7.42 (U), 20.33 (UB), 14 (PA), 3.83 (OB), and 5.08 (NA). Note that highly oscillatory upstream meniscus become nodular that can disrupt cross-web film uniformity.[12] [Color figure can be viewed in the online issue, which is available at wileyonlinelibrary.com.]

a fixed operating condition, such as flow rate and web speed, lead to changes in pressure gradient under the die lip. Changes in the upstream coating bead pressure gradient shift the upstream meniscus location. This shift can affect operating limits associated with the meniscus location, such as weeping or bead breakup, thereby changing the coating window. When the flow rate and the minimum gap height is fixed as depicted in Figure 3, the weeping can occur at higher vacuum pressure and the bead breakup can occur at lower vacuum pressure for tilted die configuration, except in case of a small positive angle, that is, $0 < \theta_a \lesssim 2^\circ$.

The attack angle also increases the strength of adverse pressure gradient in either positive and negative angles. As one can see in Figures A3 and A4, large magnitude in both angles always leads to the appearance of vortices under the downstream die lip, which can be created by reversal flow due to a strong adverse pressure gradient. Note that the vortices can suspend particles in the coating solution long enough to induce unwanted flocculation and coagulation.[8] The size of the vortices for PA is larger than that for NA, which implies a stronger adverse pressure gradient. Therefore, PA may be susceptible to ribbing instability,[25] which is typically observed when the downstream meniscus is near the diverging channel with a strong adverse pressure gradient.

The computational analysis of thickness variation under on-going periodic disturbances reveals the effect of a tilted layout. According to the flow rate disturbance results, the pressure gradient oscillation under the downstream die lip determines the film thickness variation. The strength of the pressure gradient oscillation is strongly affected by the flow apportioning, that is, separation of flow from the feed slot to upstream and downstream coating beads. The amount of the flow rate directly toward the downstream coating bead, which is responsible for the downstream pressure gradient oscillation, can be adjusted by either (1) increasing the flow rate toward the upstream when the total flow rate is fixed, or (2) decreasing the total flow rate. This flow apportioning can be controlled by the die configurations. The configuration that provides larger upstream bead volume per unit width at the same bead length, such as OB or NA, leads to smaller film thickness fluctuations. The die tilting, especially with the attack angle considered in this study, leads to amplification factors which are comparable to corresponding underbite or overbite die configurations. When an OB is not available, one may attempt to tilt the die in a negative angle direction to suppress flow rate oscillation.

To understand the film thickness uniformity on the downweb direction under gap oscillation, free surface and web oscillations must be considered separately. Interplay between the amplitude and the phase lag of the free surface oscillation turns out to be the most critical factor for the thickness variation. Although the effect of die configuration for the free surface oscillation amplitude in the gap oscillation is larger than that of the flow rate oscillation around the frequency between 2 and 500 Hz, the phase lag increases rapidly and becomes dominant toward the high-frequency regime. Therefore, the optimal die configuration (UB) having a low thickness amplification factor at low frequency ($\sim$10 Hz) is different from the optimal die configuration (OB) at high frequency ($\sim$200 Hz). Considering all aspects of the gap oscillation, the NA configuration is a reasonable choice. Although it does not have the smallest film thickness variation, it is reasonably small over all frequency ranges. Furthermore, the configuration has the smallest upstream meniscus oscillation.

In this study, the downstream free surface was pinned at the downstream die corner. When the coating liquid wets the die shoulder, however, we are expecting that the pattern of the downstream free surface oscillation, especially the phase lag, will be changed. This issue is currently under detailed investigation.

Acknowledgments

This research was supported by the Basic Science Research Program through the National Research Foundation of Korea (NRF) funded by the Ministry of Science, ICT, & Future Planning (Grant No. NRF-2013R1A1A1004986). This work was supported by LG Chem (No. AP1400056).

Literature Cited

1. Beguin AE. Method of coating strip material. *US Patent* 2,681,294, 1954.
2. Ruschak KJ. Limiting flow in a pre-metered coating device. *Chem Eng Sci*. 1976;31:1057–1060.
3. Higgins BG, Scriven LE. Capillary pressure and viscous pressure drop set bounds on coating bead operability. *Chem Eng Sci*. 1980; 35:673–682.
4. Carvalho MS, Kheshgi HS. Low-flow limit in slot coating: theory and experiments. *AIChE J*. 2000;46:1907–1917.
5. Lee KY, Liu LD, Liu TJ. Minimum wet thickness in extrusion slot coating. *Chem Eng Sci*. 1992;47:1703–1713.
6. Chang YR, Chang HM, Lin CF, Liu TJ, Wu PY. Three minimum wet thickness regions of slot die coating. *J Colloid Interface Sci*. 2007;308:222–230.
7. Lin CF, Wong DSH, Liu TJ, Wu PY. Operating windows of slot die coating: comparison of theoretical predictions with experimental observation. *Adv Polym Technol*. 2010;29:31–44.
8. Nam J, Scriven LE, Carvalho MS. Tracking birth of vortex is flows. *J Comput Phys*. 2009;228:4549–4567.
9. Nam J, Carvalho MS. Flow in tensioned-web-over-slot die coating: effect of die lip design. *Chem Eng Sci*. 2010;65:3957–3971.
10. Joos FM. A simple model of frequency response for slot coaters. In: 3rd Annual European Coating Symposium. Erlangen, Germany: University of Erlangen Nuremberg, 1999.
11. Christodoulou KN. Computational physics of slide coating flow. Ph.D.Thesis, Ann Arbor, MI: University Microfilms International, 1990.
12. Gates ID. Slot coating flows: feasibility, quality. Ph.D.Thesis, Ann Arbor, MI: University Microfilms International, 1999.
13. Tsuda T, deSantos JM, Scriven LE. Frequency response analysis of slot coating. *AIChE J*. 2010;56(9):2268–2279.
14. Lee S, Koh H, Ryu B, Kim S, Jung H, Hyun J. Operability coating windows and frequency response in slot coating flows from a viscocapillary model. *Chem Eng Sci*. 2011;66:4953–4959.
15. Romero OJ, Carvalho MS. Response of slot coating flows to periodic disturbances. *Chem Eng Sci*. 2008;3:2161–2173.
16. Perez EB, Carvalho MS. Optimization of slot-coating processes: minimizing the amplitude of film-thickness oscillation. *J Eng Math*. 2011;71:97–108.
17. Gutoff EB, Edward DC, Mujumdar AS. *Coating and Drying Defects*. Hoboken, New Jersey: Wiley, 1995.
18. Tracton AA. *Coatings Technology Handbook*, *3rd ed*. 6000 Broken Sound Parkway NW, Suite 300: CRC Press, 2006.
19. Sartor L. Slot coating: fluid mechanics and die design. Ph.D.Thesis, Ann Arbor, MI: University Microfilms International, 1990.
20. Lee S, Kim S, Nam J, Jung H, Hyun J. Effect of sloped die lip geometry on the operability window in slot coating flows using viscocapillary and two-dimensional models. *J Coat Technol Res*. 2014;11(1):47–55.
21. Bolstad JH, Keller HB. A multigrid continuation method for elliptic problems with folds. *SIAM J Sci Stat Comput*. 1986;7(4):1081–1104.
22. O'Brien WG. Beveled edge metered bead extrusion coating apparatus *US Patent 4,445,458*, 1984.
23. Arsten NJ, Buskens PJP, Rooijmans M. Slot coating die configuration. *EP patent 0,650,769*, 2000.
24. Tokimasa Y, Tsuji A. Coating method and coater. *US Patent App 10/858,369*, 2004.
25. Pearson JRA. The stability of uniform viscous flow under rollers and spreaders. *J Fluid Mech*. 1960;7:481–500.

Appendix A

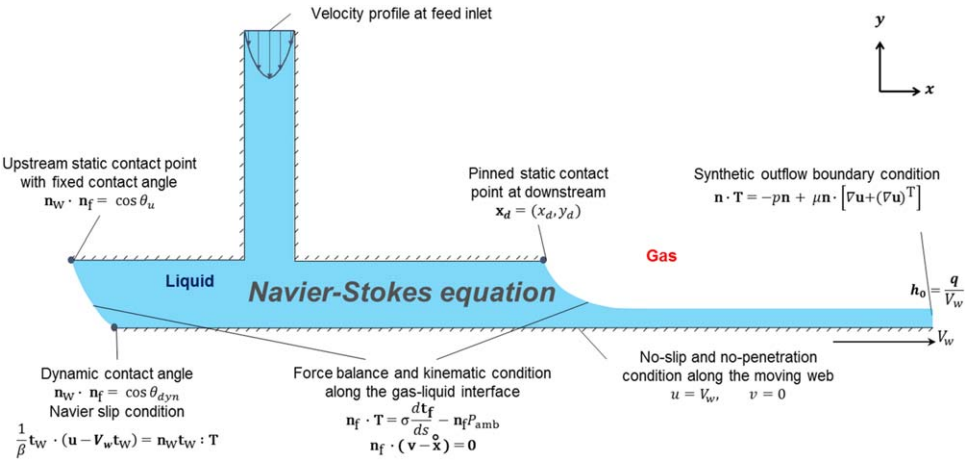

Figure A1. Boundary conditions for the slot coating model.

[Color figure can be viewed in the online issue, which is available at wileyonlinelibrary.com.]

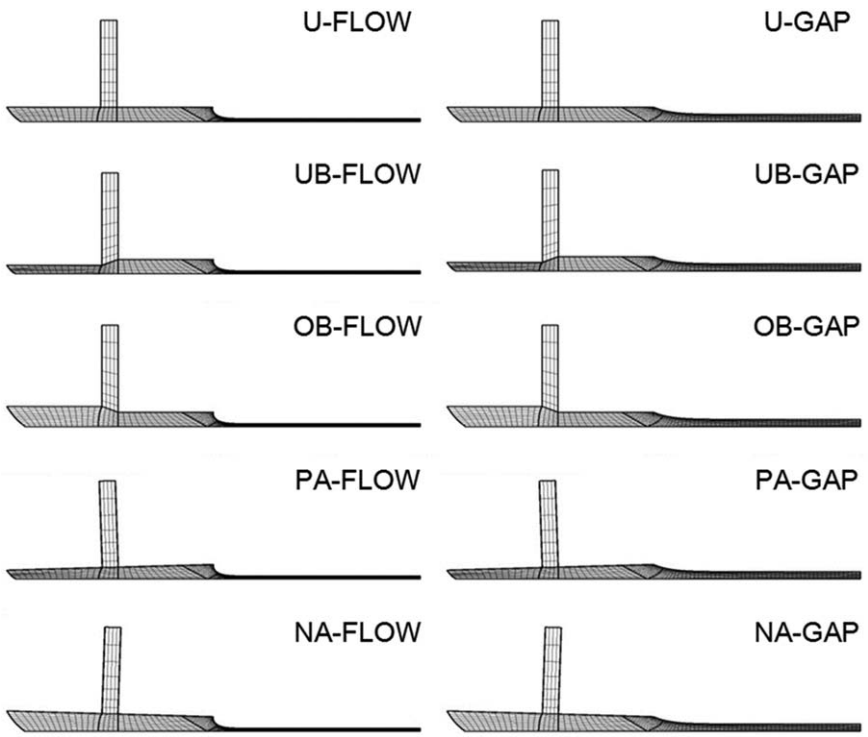

Figure A2. Finite-element mesh used with 1194 (left) and 1108 (right) quadrilateral elements for each configuration: uniform (U), underbite (UB), overbite (OB), positive angle (PA), and negative angle (NA).

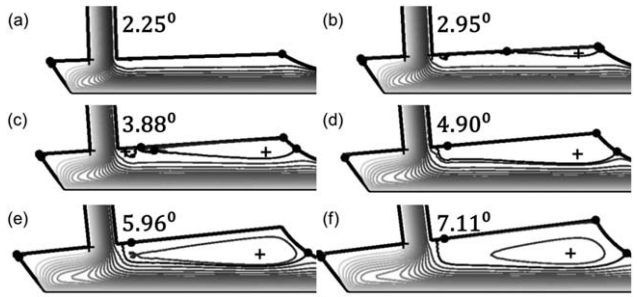

Figure A3. The birth of a vortex in the PA configuration with respect to the attack angle.

The flow conditions are $N_{Ca} = 0.05$, $N_{Re} = 0$, $R_{gt} = 2$, and $P^*_{vac} = 0.83$.

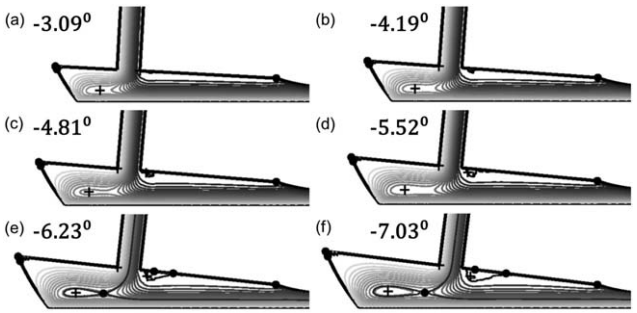

Figure A4. The birth of a vortex in the NA configuration with respect to the attack angle.

The flow conditions are the same as in Figure A3.

Manuscript received Sep. 25, 2014, and revision received Dec. 20, 2014.